



1 Earthquake-induced landslides monitoring and survey by means of 2 InSAR

3 Tayeb SMAIL¹, Mohamed ABED¹, Ahmed MEBARKI^{2,3}, Milan Lazecky^{4,5}

4 ¹Department of Civil Engineering, Saad Dahlab University, Blida City, Algeria

5 ²University Gustave Eiffel, Laboratory Multi Scale Modeling and Simulation (UMR 8208 CNRS/UPEC/U.Eiffel), 5 Bd
6 Descartes, 77454, Marne-La-Vallee, France

7 ³Nanjing Tech University, 5 New Mofan Rd, Gulou, Nanjing, Jiangsu, Chine - Permanent Guest Professor within “High-
8 Level Foreign Talents Programme” grant

9 ⁴IT4Innovations, VSB-TU Ostrava, 17, Listopadu 15, 70833 Ostrava-Poruba, Czech Republic

10 ⁵School of Earth and Environment, University of Leeds, Leeds LS2 9JT, UK

11 *Correspondence to:* SMAIL Tayeb (st_gc@hotmail.fr)

12 **Abstract.** This study uses interferometric SAR techniques to identify landslides and lands prone to landslides, detect fringes
13 and changes in areas struck by earthquakes. The pilot study investigates the Mila region (Algeria) which suffered significant
14 landslides and structural damages (earthquake: Mw 5, 2020-08-07): the study checks ground deformations and tracks
15 earthquake-induced landslides. DInSAR analysis shows normal interferograms, with atmospheric contribution, and slight
16 fringes. However, it identifies many landslides, the most important (2.5 m displacement) being located in Kherba
17 neighborhood, causing severe damages to dwellings. In addition, SAR images and optical images (Sentinel-2) confirm site
18 investigations. Although in Grarem City, optical images could not detect any disorder, the DInSAR analysis detected some
19 coherence decays and small fringes (3.94 Km² area). These unnoticed ground disorders were confirmed during fields
20 inspection. Such results have key importance since they can serve as an alert to monitor the zone at the proper time.
21 Furthermore, Displacement time series analysis of many interferograms (April 2015 to September 2020) using LiCSBAS were
22 performed to investigate the pre-event conditions and precursors of the slopes instabilities., LiCSBAS detects a line-of-sight
23 subsidence velocity of -110 mm/y in the back hillside of Kherba, and high displacement velocity at specific points in Grarem
24 region.

25 1 Introduction

26 Although it is still challenging to predict exactly where and when natural hazards (earthquakes, landslides, floods, etc.) might
27 occur, the capacity to monitor and survey the zones prone to important landslides as well as the capacity to identify and locate
28 those impacted by earthquakes are key issues in risks mitigation, reduction, preparedness and adaptation. Actually, since
29 earthquakes and landslides might occur in many places worldwide, they might cause a huge number of victims, important
30 socio-economic, assets damages and losses. Their impact can be significantly reduced thanks to satellite imaging which allows
31 prediction and early alerts of some landslide cases (Jacquemart and Tiampo, 2021).

32 It is then worth detecting or predicting critical ground changes at specific places, either after a geotechnical disorder occurs
33 due to landslides and earthquakes mainly, or before it is suddenly triggered (Bakon et al., 2014; Galve et al., 2015). Such
34 challenges can be tackled by regular image processing oriented landslides areas monitoring, in the aftermath of earthquakes,
35 by means of SAR interferometric methods and optical images, for instance. Actually, since InSAR (Interferometric Synthetic
36 Aperture Radar) is an active sensor system that uses microwave signals to collect data backscattered from the earth's surface,



37 the use of satellite imaging systems InSAR appears as a cost-effective way for measuring millimeter-level displacements of
38 the earth surface (Herrera et al., 2009), at a regional scale and can be used as an early warning system for the safety of structures
39 and their surroundings (Galve et al., 2015; Roque et al., 2015).

40 The expected outcomes are based upon the processing of SAR data making use of Differential InSAR (DInSAR),
41 Coherence Change Detection (CCD) and time series analysis of LiCSAR dataset using LiCSBAS software, to illustrate the
42 advantages of high-resolution SAR sensing for the objective of tracking ground changes and landslides.

43 The performed SAR analyses can reveal some ground changes detected through DInSAR and CCD maps, as it is shown
44 the illustrative purposes for the 7th of August 2020 earthquake (Algeria, Mila). These displacements, in the northeastern part
45 at the Grarem City (2 km from Mila downtown) and Kherba City, caused a loss of coherence in CCD and fringes in DInSAR
46 maps. Their extend affects areas of around 3.94 km² for Grarem and 2.1 km² for the Kherba landslide area. Furthermore, the
47 time-series analysis using LiCSBAS reveals a slow deformation signal in the left part of Kherba landslide area.

48 The formed fringes and coherence loss in Grarem case indicate the boundary of a potential land failure. The results can
49 serve as early warning information provided by the InSAR monitoring system, since the area should be monitored to investigate
50 the existent or probable growing disorder.

51 **2 Land and ground movements monitoring and surveying in the aftermath of an earthquake**

52 **2.1 Satellite images and methods - Case study**

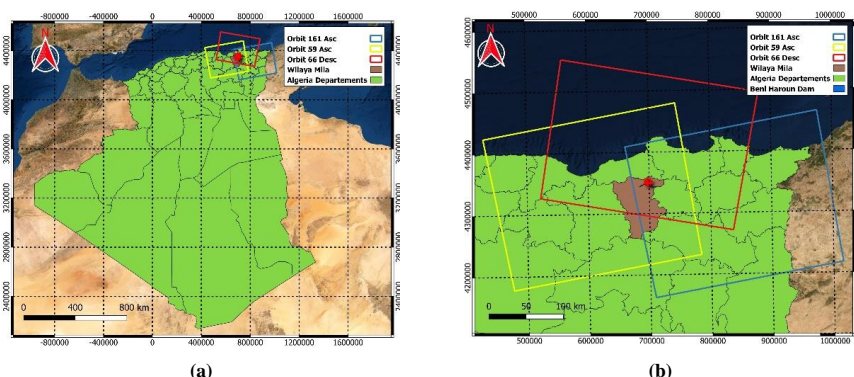
53 The present research study is multifold. It aims to use InSAR image processing for various purposes, in the case of landslides
54 and earthquakes:

- 55 - Use the InSAR in the aftermath of an earthquake in order to identify the geotechnical disorders, their extent and
56 locations. The Differential radar interferometry and the Coherence Changes Detection are the most adapted methods
57 for ground and soil surfaces changes detection (Jung and Yun, 2020; Meng et al., 2020; Pawluszek-Filipiak and
58 Borkowski, 2020; Tampuu et al., 2020; Tzouvaras et al., 2020). A city, Mila, in Northern Algeria, is considered as the
59 pilot study. It has been struck by an earthquake in August 2020. The geotechnical disorders (landslides and surface
60 faults) have affected significantly, during the same earthquake events series, two distinct zones being distant by almost
61 15 km from each other.
- 62 - Use the time series analysis to study the mean displacement and mean velocity before and after the occurrence of the
63 main shock. For the city of Mila, the time series is performed out for a period extending from April 2015 up to October
64 2020, i.e. a long period before the (*April 2015 up to March 2020, i.e. 5 entire years*) and a period *4 months* ahead of
65 the main shock in order to avoid a disturbance or bias that might be related to seasonal effects such as rains and
66 vegetation effects (Lazec̆ky et al., 2020a).
- 67 - Compare and correlate the InSAR images processing results with the satellite optical images observations.

68 **2.2 Pilot zone, earthquakes and landslides - Observed disorders**

69 The case study area lies in Mila Province which is located in the northeast part of Algeria (Mediterranean zone), near the Dam
70 of Beni Haroun. The Mediterranean zone is seismically active because of the northward convergence (4-10 mm/yr) of the
71 African plate relative to the Eurasian plate along a complex plate boundary (USGS). Throughout the last years, several
72 landslide events have taken place in the wider region of Mila. The seismic activities and landslides pose a persistent threat for
73 built-up areas and facilities, such as roadways, bridges and tunnels, which need continuous monitoring and survey.

74 After an earthquake (Mw 5, 2020-08-07, epicenter 36.550° N - 6.271° E, Depth=10 km, (USGS)struck this region,
75 important landslides were mostly observed in Mila City and its surroundings, see Figs. 1 and 2. Although, the earthquake was
76 moderate, Beni Haroun Dam and the two large bridges built on the RN 27 highway needs to be inspected and their possible
77 displacements monitored.



78
 79
 80
 81

Figure 1. Mila location map (a), ascending and descending orbits footprints. Red stars indicate earthquake epicenter (QGIS, ESRI basemap).

82 In the present, two areas are studied, i.e. Kherba and Grarem Cities. The altitude at the top point 1 (Fig. 4.a) in Kherba hill
 83 is 654 m and 411 m a.s.l. in the upper point (2), with a horizontal length between 2.14 km and a slope of 11.34%. The maximum
 84 ground horizontal offset reached 2.5 m and the vertical deformations exceed 1.8 m (Fig. 2.b) at the top of Kherba hill (point A
 85 Fig. 4.a). The slope failure boundary of Kherba City is mapped as shown in Fig. 4.b. The Grarem area of interest (AoI) is
 86 located at east north of Mila in a hilly ground with an average slope reaching 12.5%, see Fig. 4.c.



87
 88
 89
 90

Figure 2. Ground cracks due to landslides in Kherba, Mila, ~2.5m offset towards the North, a. Drone aerial photo from (LNHC), b. & c.- Lateral displacements (Photos: courtesy M. Yacoub A., University of Setif, Algeria).

91 2.3 Pilot zone - Data and images collection

92 The dataset used for this study is collected from European Space Agency (ESA), via the Copernicus Open Access portal, and
 93 from the Alaska Satellite Facility (ASF DAAC). The C-band Sentinel-1 A and B, launched in 2014 and 2016 respectively,
 94 provide regular data sets (Morishita, 2021). For the InSAR use, the Interferometric Wide (IW) swath Single Look Complex
 95 (SLC) data is selected and processed with the open-source software SNAP (Sentinel Applications Platform). It is worth using
 96 data from many orbits to monitor the AoIs due to different oriented directions, incidence angles of satellites, and the ground
 97 topography. The optical images of Sentinel-2 sensors are obtained from ESA, whereas downloading and processing data is
 98 done via QGIS, Semi-Automatic Classification Plugin (SCP).

99 For Mila region, the AoI is covered by 3 orbits (2 ascending and 1 descending 66, 59, and 161) (Fig. 1). Since the present
 100 study intends to detect the areas influenced by landslides, many pre-event and post-event data are used in order to get an
 101 accurate evaluation of the event. Eighteen Sentinel-1 A and 17 Sentinel-1 B (total of 35) images downloaded for the period of
 102 1 July 2020 to 26 October 2020, to monitor Mila's area, are used to perform out a detailed study on the land deformation and
 103 the dynamics of the landslide. Table 1 summarizes the appropriate interferograms with a small perpendicular baseline and
 104 short temporal baseline. Tables 1-2-2bis summarize the whole data collected for the case study.

105 **Table 1.** Characteristics of Sentinel-1 InSAR pairs for Mila case.



IFG-ID	Track	M Date	S Date	Bp [m]	Bt [days]
IFG-1		2020-07-22	2020-07-28	-9.99	6
IFG-2		2020-07-28	2020-08-03	40.62	6
IFG-3		2020-08-03	2020-08-09	-51.47	6
IFG-4		2020-08-03	2020-08-09	-50.76	6
IFG-5		2020-08-09	2020-08-15	-27.57	6
IFG-6		2020-08-09	2020-08-15	27.62	6
IFG-7		2020-08-15	2020-08-21	-16.19	6
IFG-8	66 ASCENDING	2020-08-21	2020-08-27	42.43	6
IFG-9		2020-08-27	2020-09-02	-28.59	6
IFG-10		2020-09-02	2020-09-08	29.26	6
IFG-11		2020-09-08	2020-09-14	17.95	6
IFG-12		2020-09-14	2020-09-20	-6.05	6
IFG-13		2020-09-20	2020-10-02	-4.64	12
IFG-14		2020-10-02	2020-10-14	18.13	12
IFG-15		2020-10-14	2020-10-26	-49.36	12
IFG-16		2020-07-27	2020-08-02	69.64	6
IFG-17		2020-08-02	2020-08-08	-75.10	6
IFG-18	59 ASCENDING	2020-08-08	2020-08-14	-8.86	6
IFG-19		2020-08-14	2020-08-20	175.97	6
IFG-20		2020-08-20	2020-08-26	-226.75	6
IFG-21		2020-07-22	2020-07-28	-169.19	6
IFG-22		2020-07-28	2020-08-09	30.39	12
IFG-23		2020-07-28	2020-08-03	99.88	6
IFG-24	161 DESCENDING	2020-08-03	2020-08-09	-70.12	6
IFG-25		2020-08-09	2020-08-15	2.14	6
IFG-26		2020-08-15	2020-08-21	121.22	6
IFG-27		2020-08-21	2020-08-27	-196.82	6

106 **Bt**: temporal baseline; **Bp**: perpendicular baseline.

107 All-time interval for InSAR pairs processing is 6 days, except the last three pairs of the 66 ascending pass that have 12 days.
 108 Furthermore, since a bad coherence map of the IFG-24, may lead to misinterpretation of results, early images before the 3rd of
 109 August with a time interval of 12 days are selected for the co-event interferogram for the 161 descending pass (IFG-22). The
 110 gray cells in Table 1 represent the co-event interferograms. The perpendicular baselines guarantees also a good quality of
 111 InSAR studies (Braun, 2019). As LiCSBAS time series analysis aims to investigate long period displacements and velocities
 112 over a large area, 34 IFGs from the orbit 66 and 190 IFGs for the 161 ascending track (Table 2) are selected for the present
 113 study.

114 **Table 2.** LiCSAR frames, analyzing periods and the total number of IFGs used in this study.

Frame ID	Date		Period	IFGs
	Start	End		
161A_05343_090806	2015-4-26	2020-9-26	66 month	190
066D_05394_131311	2020-4-5	2020-9-26	6 months	34



115 **Table 2bis.** Sentinel-2 optical images collected for the study case.

Frame ID	Date	Duration days, to the main shock
Image 1	2020-07-30	-7 days
Image 2	2020-08-09	+ 2 days

116 **3 Methodology description and results**

117 Four aspects are investigated and compared in the present case study:

- 118 - The SAR Interferometric (InSAR) methodology, which is subdivided into three sub-groups:
- 119 - DInSAR for the phase changes (fringes),
- 120 - CDD for the coherence change detection,
- 121 - Time series analysis and LiCSAR data.
- 122 - The optical image processing.

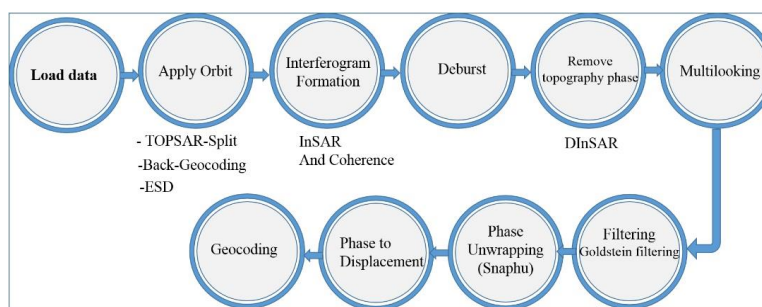
123 **3.1 SAR Interferometric methodology**

124 The Interferometric Synthetic Aperture Radar (InSAR) is an active microwave imaging system. It is independent of sunlight
 125 and can penetrate clouds, unlike optical imaging systems which are passive. InSAR uses the phase components of co-registered
 126 SAR images of the same pixel to estimate the topography and to measure the surface change in the target area (Kim, 2013).
 127 At least two constellation images are needed to generate an interferogram, which contains topographic, atmospheric effect,
 128 baseline error, and noise components (Goudarzi, 2010; Kim, 2013; Netzband et al., 2007):

129
$$\phi = \phi_{disp} + \phi_{flat} + \phi_{topo} + \phi_{atm} + \phi_{orbit} + \phi_{noise} \quad (1)$$

130 Where ϕ_{disp} is the LOS displacement, ϕ_{flat} the flat earth phase, ϕ_{topo} the topographic phase, ϕ_{atm} is an atmospheric phase,
 131 ϕ_{orbit} , the baseline phase and ϕ_{noise} is noise phase contribution (Kim, 2013).

132 The main steps for the study, by using SNAP software (DInSAR and CCD), are depicted in Fig. 3. It's worth notice that
 133 for CCD processing, it is not necessary to follow the whole (DInSAR, Phase Unwrapping, and Phase to displacement).



134
 135 **Figure 3.** Workflow chart for DInSAR processing using (SNAP) software.

136 **3.1.1 Differential radar interferometry (DInSAR)**

137 Differential radar interferometry (DInSAR) exploits the phase difference to measure coherent changes or deformation between
 138 two image acquisitions. It is often used for ground subsidence measurement(Canaslan Çomut et al., 2020; Galve et al., 2015).
 139 One of DInSAR's limitations is that the changes are not measurable in case of non-coherent events (e.g., rapid landslide)
 140 (Braun, 2019).

141 **3.1.2 CCD Times series analyses**



142 The estimated coherence is considered as a quality indicator of an interferogram (Jacquemart and Tiampo, 2021). Actually, it
143 indicates that the phase and amplitude of the received signal express the degree of similarity between the images pair. The
144 pixel coherence γ of two SAR images is estimated on the basis of N neighboring pixels (Jia et al., 2019; Wang et al., 2018).

$$145 \quad \gamma = \frac{\sum_{i=1}^N S_{1i} S_{2i}^*}{\sqrt{\sum_{i=1}^N |S_{1i}|^2 \sum_{i=1}^N |S_{2i}|^2}} \quad (2)$$

146 Where: S_{1i}, S_{2i} , are the complex signal values of the SAR image pair, N is window of neighboring pixels, $*$ is the complex
147 conjugate.

148 The coherence values range between 0 and 1 so that the map is represented as a gray color which 0 is white and 1 is black.

149 3.1.3 Time series analysis and LiCSAR data

150 The LiCSAR system processes Sentinel-1 InSAR datasets, and generates wrapped, unwrapped interferograms and coherence
151 maps (Lazecký et al., 2020b), with a final product resolution of ~ 26.5 m (Lazecký et al., 2020a). For such purposes, the open-
152 source LiCSBAS software, adopted in the present study, is used for InSAR time series analysis based on LiCSAR data. It is
153 able to generate maps of mean velocity displacement and deformation time series for all processed frames. Furthermore, it is
154 easy to implement and does not request high-performance computing facilities (Morishita, 2021).

155 In addition, the mechanism of landslides can be thoroughly studied through LiCSBAS analyses. They rely on the InSAR
156 time-series analysis package integrated with Looking into Continents from Space with Synthetic Aperture Radar (LiCSAR),
157 (Lazecký et al., 2020b). Such time series analyses are very helpful in identifying, for a given landslide or geological disorder,
158 the prior patterns of ground movements versus the time as well as foreseeing a potential disorder.

159 3.2 Optical image processing

160 The optical methods are a passive detection way that needs sunlight and clear weather conditions in order to exploit the data.
161 The optical data collected from the ESA platform (Sentinel-2) is treated and plotted using QGIS, in the present study.

162 4 Application to the case study and results

163 The case studies are located in two different sites and both areas of interest are located in Algeria. They have a hilly relief: the
164 first one is located northeast of Mila City (Grarem) and the second is at the west part of Mila City (Kherba). To monitor the
165 AoIs, several available images are processed and used with different orbits directions (Ascending and Descending, see Fig. 1),
166 in order to catch deformation from different angles along the sensor's LOS. The InSAR technique is used in both areas, in
167 order to detect land deformation and landslides caused by the earthquake.

168 The present study uses Sentinel-1 A and B datasets: The Sentinel-1 sensors have a wavelength of 5.546 cm (ESA) and are
169 right side-looking with an incidence angle ranging approximately from 20° to 46° (ESA, 2012), which are suitable for change
170 detection and the monitoring of large areas. Furthermore, optical sensors data from Sentinel-2 are used in order to validate the
171 ground changes detected by InSAR.

172 The four adopted methods are applied for Mila case study in order to:

- 173 - detect and measure the co-event surface displacements and landslides, caused by the earthquake (CCD and DInSAR)
- 174 - monitor their dynamic evolution in the first weeks and months, at the post-event period (CCD and LiCSAR data)
- 175 - analyze their possible initiation ahead of the earthquake by months and years, at the pre-event period (Time-series
176 methods and LiCSAR data)
- 177 - corroborate the results by comparing several methods outputs, i.e. SAR (CCD, DInSAR, LiCSAR), aerial optical photo
178 (Sentinel-2), and field surveys.

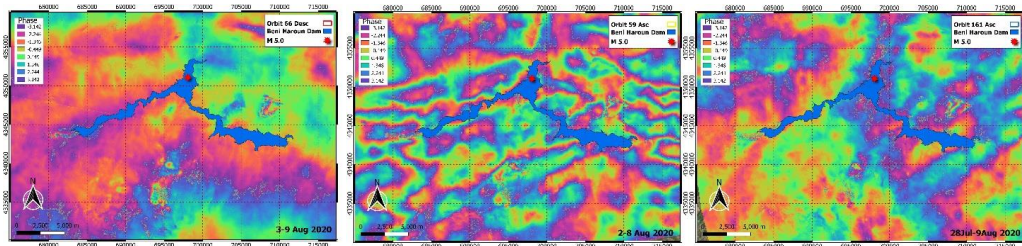


179 The quality of the SAR image is consistent with the topography slopes and area roughness. Actually, the AoI has rough
180 topography, hills, and rivers. Selecting either ascending or descending passes, relying on which will avoid some limitation of
181 InSAR is an extremely essential action able to infer the deformation from various angles. Therefore, considering the regional
182 topography and geology of the AoI is necessary to process InSAR and results interpreting.

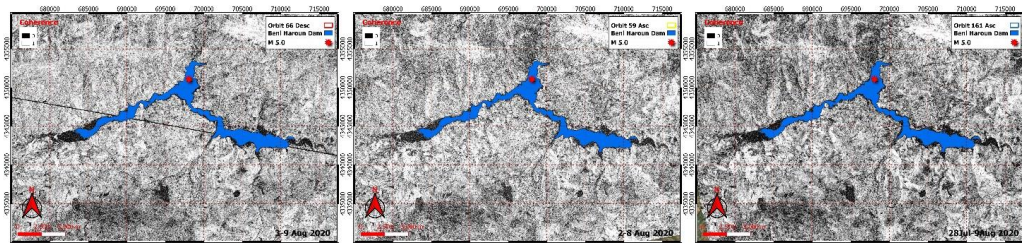


183
184
185 **Figure 4.** 3D view of AoIs, Kherba AoI and Grarem using QGIS with DEM SRTM 1sec and ESRI basemap, a & b are Kherba AoI, c is
186 the Grarem case area, the red polygon is the boundary of change detected by InSAR.

187 Differential InSAR (DInSAR) method is helpful to investigate co-seismic effects and detect changes in the ground. The
188 produced Interferograms and coherence images are projected to WGS84 reference, with a pixel size of 13.4 m. The unwrapped
189 interferograms present phase contribution of many noise resources (atmospheric), see Fig. 5. In general, strong earthquakes
190 cause large-scale fringes patterns around the epicenter which is not the case in the event under study (a moderate earthquake).
191 Processing DInSAR analysis may then lead to misinterpretation due to atmospheric contribution in differential phase
192 interferograms (Fig. 5). In the study case, no regional deformation due to the earthquake is observed and there is no need to
193 continue investigating the dam and the two bridges by simple DInSAR. However, this moderate earthquake has triggered small
194 deformation and landslides in Grarem, Kherba, and Azeba, see Figs. 7, 10, and 20.



195
196 **Figure 5.** Wrapped Interferograms from Sentinel-1 for IFG-3+IFG-4, IFG-17 and IFG-22, The red star is the epicenter location USGS.



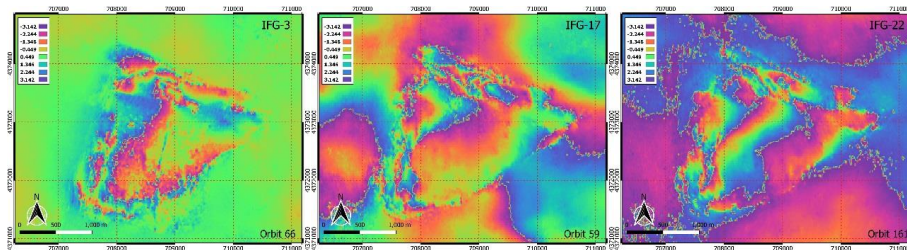
197
198 **Figure 6.** Mila Area, InSAR coherence maps for IFG-3+IFG-4, IFG-17 and IFG-22.

199 The IFG-3 and IFG-4 are merged in one image due to the AoIs, which are located between two different image acquisitions
200 in orbit number 66. In order to monitor the dam and bridges, it is highly recommended to use PS-InSAR for regional and local
201 ground deformation detection (Hooper et al., 2004; Rapant et al., 2020; Sanabria et al., 2014).

202 4.1 Case of GRAREM

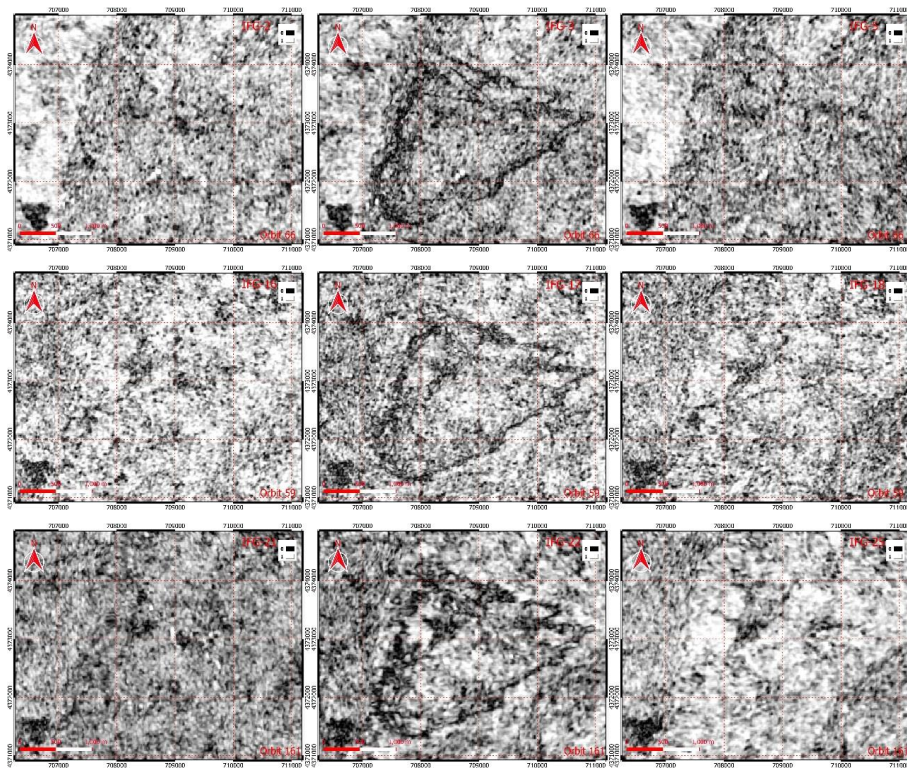


203 The detection of deformation or changes between two InSAR images reveals a small change in the region of Grarem. This
204 change is detected as small fringes, each fringe corresponding to a displacement of a half-wavelength ($\lambda=5.546$ cm) in the LOS
205 direction (Fig. 7). Usually, coherent change does not appear in coherence images as dark region, but in the study case, the
206 outer borderline of the fringes region shows incoherence change which is clearly visible in coherence maps (Fig. 8).



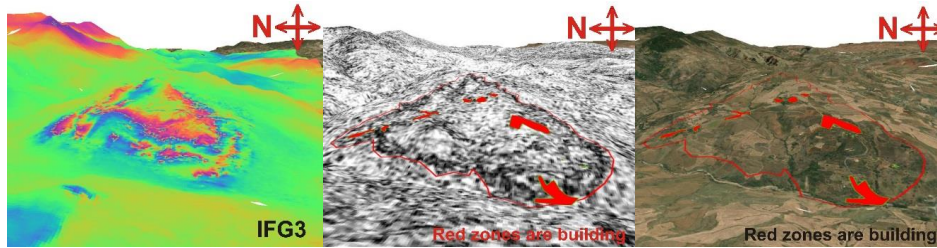
207
208 **Figure 7.** Detected fringes in Interferograms N° 3, 17 and 22, focus images on Grarem zone.

209 A time series analysis needs then to be performed out to prove whether this contour was formed at the event occurrence
210 date (August 7, 2020). The coherence maps present a dark polygon which is related to incoherent change or deformation. But
211 inside the AoI, the results show a coherent change which means that this area has deformed as a block up or down.



212
213
214 **Figure 8.** Coherence maps of Grarem AoI: the images represent pre-event, co-event and post-event for each orbit.

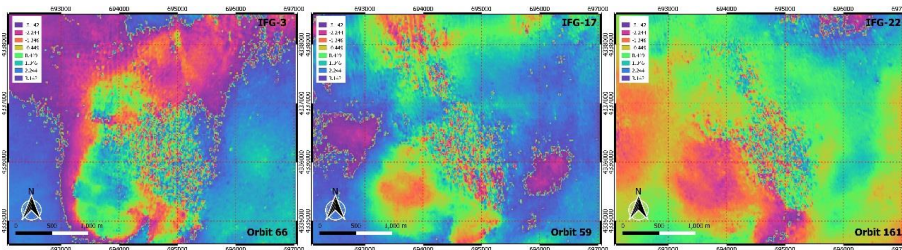
215 The affected area covers about 3.94 km² as estimated from phase and coherence maps, with an average runout distance from
216 the top to downhill of 2.6 km.
217



218
219 **Figure 9.** 3D view of Grarem Area, Images of IFG-3. Each fringe = wavelength/2 in LOS, and red zones represent existing building
220 compounds (QGIS, ESRI basemap).

221 4.2 Case of Kherba

222 DInSAR is expected to be more suitable for slow and gradual movements (Cascini et al., 2013). In the present study, Kherba's
223 landslides exceed the capabilities of DInSAR since this method cannot measure the changes due to incoherent change at the
224 first event. Phase images of the Region of Interest (RoI) show a clear decorrelation and consequently, the phase information
225 is no longer convenient for analysis.

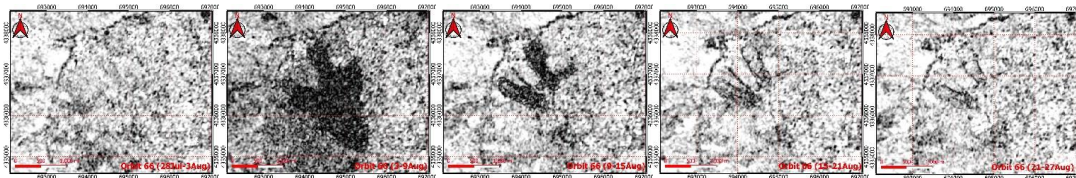


226
227 **Figure 10.** Kherba main event interferograms, biased pixels in the RoI correspond to changes.

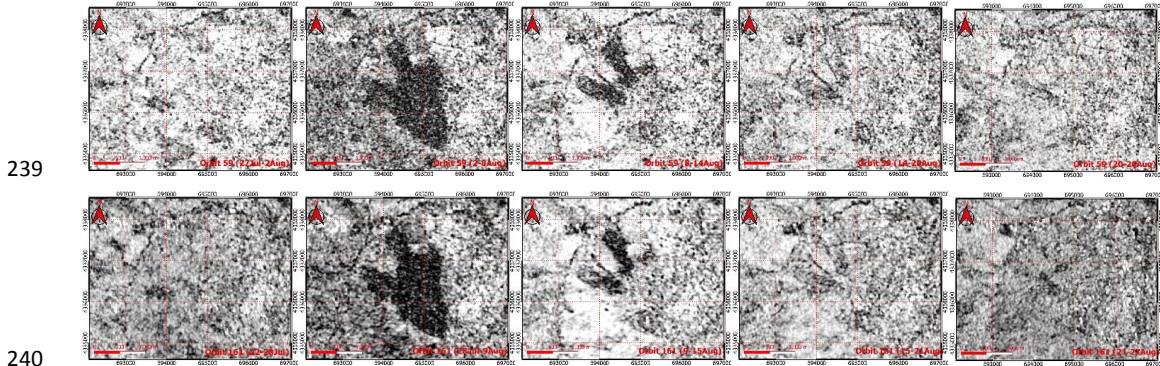
228 In such cases of incoherent changes, we can serve to the coherence change detection (CCD) method which is suitable and able
229 to monitor the event.

230 4.2.1 CCD Times series analyses

231 For the case study, the coherence maps (Figs. 11-13) show very low coherence in the area (RoI) and indicate that some
232 changes have occurred. This may confirm whether the decrease of coherence values is due to the hazard or it is naturally
233 low. The Coherence Change Detection (CCD) is useful when the change is incoherent in the scene, since CCD quantifies
234 changes between two SAR images, and is represented as a decay of coherence values. To distinguish between natural low
235 coherence (e.g., water, vegetation...) and induced surface changes, a second coherence map is needed in order to serve as a
236 reference to be compared with pre-event images. It is preferable to mask out the rest of the non-changed area with a ratio of
237 pre-event by co-event image and filter values that are equal of less than 1 (see Fig. 13).



238

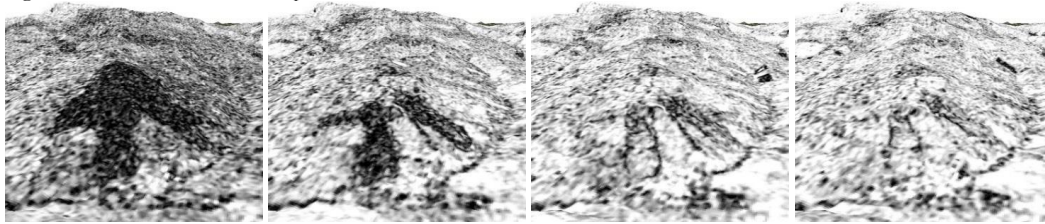


239

240

241

Figure 11. Coherence time series maps of Kherba, Sentinel-1.



242

243

Figure 12. 3D view of Kherba City, Sentinel-1 Coherence images Orbit 66.

244

The CCD time-series display the changes in the AoI over time for Kherba. The dark region represents the main changes that occurred during the co-event period. The landslide shape is divided into two toes at the lower side of the Hill, as shown in Figs. 11 and 12.

245

246

247

During the first week following the earthquake, changes are detected in the lower side of the hill, and lasted until the late date of August 2020 (IFG-8 orbits 66, IFG-27 orbit 161 and IFG-20 for orbit 59). Afterwards, many other sources of noise were present in the AoI, which makes this technique less efficient (weather, human activities). Most of the processed images are 6 days' intervals, except the orbit 161 in which the co-event image (IFG-24) was not enough good to compare with other pre-post event images: it is then replaced by the IFG-22. Figs. 14 and 15 illustrate how the image selection may change the interpretation of results.

248

249

250

251

252

253

To quantify the change, an RoI is represented in Fig. 13, and the plots in Figs. 14 and 15 shows also the calculated average coherence values and the decreased percentage values inside the RoI. For the 66 orbit's pairs, the RoI average coherence starts by 0.66 during the pre-event period (IFG-2) and decreases to 0.51 during the co-event period (-31%) (IFG-3). For orbit 59 pairs, it decreases by 27% with a mean value of 0.60 (IFG-17) after an initial mean value of 0.77 (IFG-16).

254

255

256



257

258

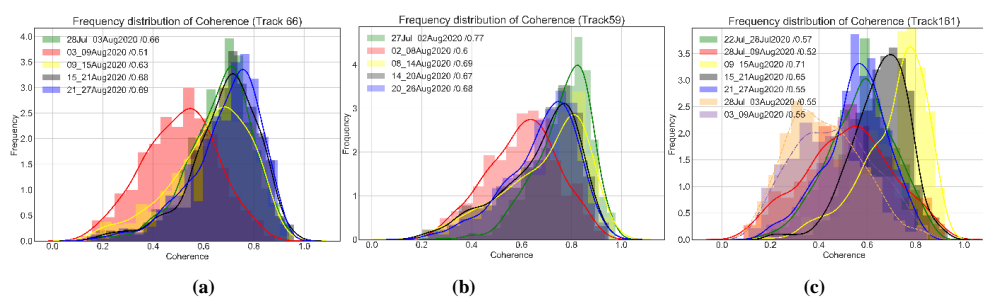
259

Figure 13. Pre-event coherences ratio (left), coherences ratio (right), Sentinel-1 Orbit 66. The green box indicates the scope of the RoI, red spots represent significant changes of coherence in the landslide region (QGIS, ESRI World Imagery basemap).

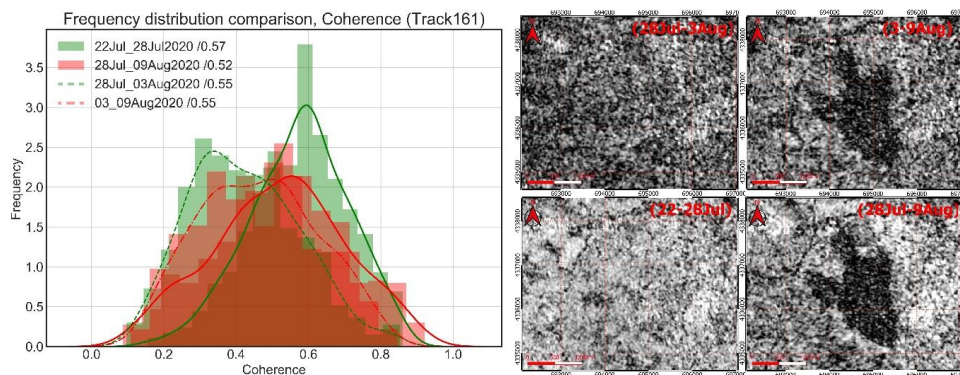


260 The last orbit 161 pairs make an exception due to an initial bad coherence map (IFG-23 and 24), see Fig. 14.c. However, the
 261 previous pair (IFG-21 and IFG-22) gave a value of 0.57 (IFG-21) which decreased to 0.52 (IFG-22), i.e. 11% of change.
 262 **Table 3.** Mean coherence change values inside the ROI.

Orbit	Pre-event coherence mean	Co-event coherence mean	Change
66	28Jul_03Aug	03_09Aug	-31%
	0.66	0.51	
59	27Jul_02Aug	02_08Aug	-27%
	0.77	0.60	
161	22Jul_28Jul	28Jul_09Aug	-11%
	0.57	0.52	



263
 264
 265 **Figure 14.** Frequency distributions of coherence values within ROI for coherence time series images.

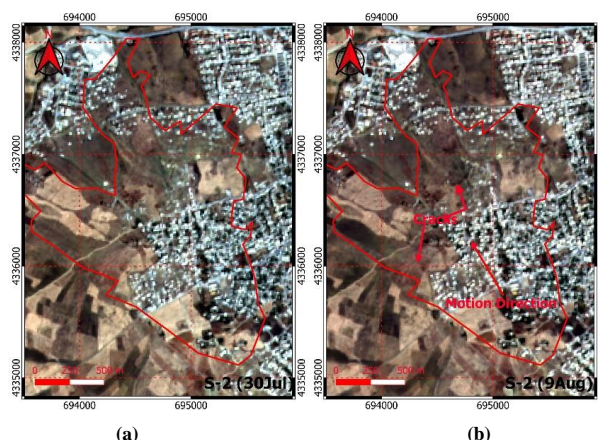


266
 267 **Figure 15.** Effect of bad coherence shift: the cause is the acquisition of 3rd August start at (17:28:15, orbit 161) under bad weather
 268 conditions in the acquisition time according to precipitation site (WVO) (rainfall in that daytime), compared to the acquisition of the same
 269 day but not the same time (05:37:58 for orbit 66).

270 The surface area covers 2.1 km², derived from the coherence images, and the shape ends by two toes. The runout distance
 271 is 2.4 km for the right toe and 2.15 km for the left one. The CCD method has the potential to differentiate between the areas
 272 impacted by induced changes and those affected by other sources of noise. The ratio operation is useful in canceling out other
 273 noise factors and improve the detection of changes in the region.

274 4.2.2 Optical detection

275 To validate the SAR methods results, two images from Sentinel-2 are downloaded and treated, the images being dated 2020-
 276 07-30 (a week before the main shock) and 2020-08-09 (two days after the main shock), and the optical data is treated using
 277 QGIS. The passive detection shows that an important ground surface displacement affected the Kherba neighborhood, over an
 278 area of 1.32 km². The landslide shape of deformation has only one toe at the lower part of the hill compared to the CCD method
 279 results.

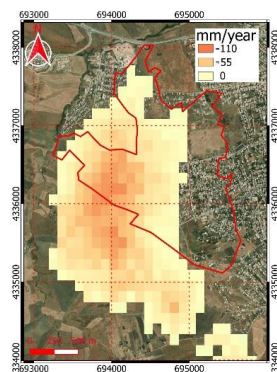


280
281
282 **Figure 16.** Sentinel-2 Optic Images: (a)- dated 30-Jul 2020, (b)- dated 09-Aug 2020.

283 4.3 LiCSBAS analyses

284 LiCSBAS is an open-source program for InSAR time series analysis based on LiCSAR data. The LiCSAR system
285 automatically processes Sentinel-1 InSAR datasets (Lazecký et al., 2020b), to generate wrapped, unwrapped interferograms
286 and coherence maps (Lazecký et al., 2020b), with a final product resolution of ~26.5 m (Lazecký et al., 2020a). LiCSBAS
287 exploits the data of LiCSAR in order to generate maps of displacement mean velocity and deformation time series plots
288 (Morishita, 2021).

289 Displacement time series and velocities analysis of the region is performed out using LiCSBAS. It allows identifying
290 whether unstable conditions pre-existed or are still undergoing. The study started from the 5th of April to the 26th of September
291 2020, for the orbit 66 and from 26 April 2015 to 26 September 2020 for the orbit N° 161.



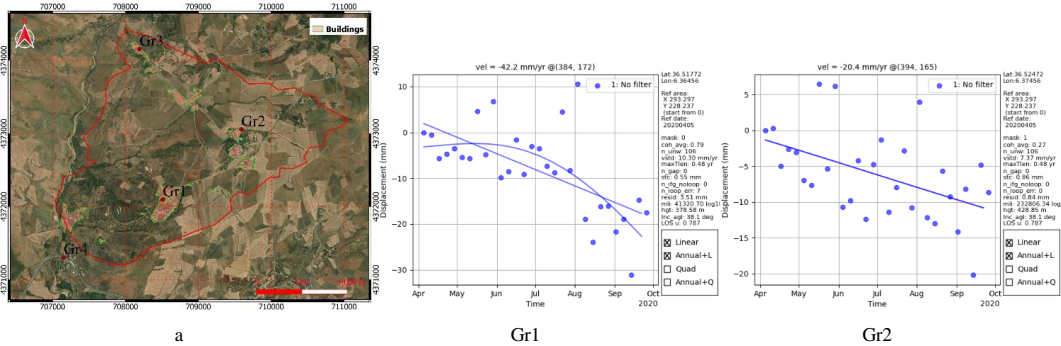
292
293 **Figure 17.** Line of sight (LOS) displacement velocity map, red line is landslide area (066D_05394_131311) (QGIS, ESRI basemap).

294 The time series detected subsidence at the west part of Kherba. This region is on the other hillside of Kherba Hill. A site
295 investigation did not find any drilled wells. One may assume that this subsidence is not due to any pumping of groundwater.
296 Therefore, another possible explanation is probably related to the mass movement of the main landslide hillside. The
297 displacement velocity in Kherba is about 110 mm/year, Fig. 17.

298 For the Grarem case, the velocity map looks stable between the same dates (April 5 to September 26, 2021). The change
299 occurred rapidly and is removed by the filters. For illustrative purposes, the displacement time series of some points are
300 illustrated in Figs. 18 and 19.



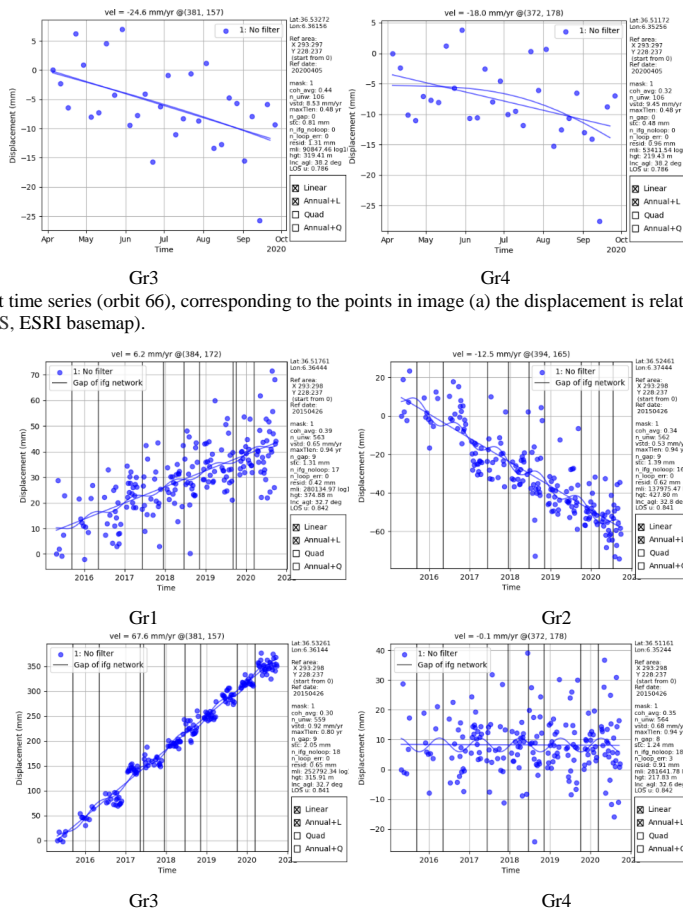
301
 302



303
 304
 305
 306

Figure 18. Displacement time series (orbit 66), corresponding to the points in image (a) the displacement is relative to the reference point, (a) Grarem region, (QGIS, ESRI basemap).

307
 308



309
 310
 311

Figure 19. Displacement time series (orbit 161), corresponding to the points in Fig. 18.a, displacement is relative to the reference point.

312
 313

During the LiCSBAS processing, a primary stable reference point is selected (36.455885° N, 6.276909° E). This method proves to be efficient for large-scale deformation monitoring and slow coherent changes.

314

4.4 Discussion

315
 316
 317

InSAR monitoring proves its ability to detect land changes. First, landslides and land deformation can be detected remotely by InSAR. Furthermore, optical images could detect only one case (Kherba). The theoretical results were validated by site visiting and investigation, i.e.:



- 318 - Compared to results obtained from optical for the Kherba landslide, InSAR is more precise for detecting small
319 deformation (2 toes in CCD maps). Besides, the other techniques did not detect the full changing area in the region (only
320 one toe).
- 321 - Landslides of this magnitude exceed the capabilities of DInSAR, and their extreme loss of coherence. The interferograms
322 of co-events are strongly decorrelated. Therefore, the phase information is no longer usable and one cannot measure the
323 displacement of incoherent ground changes (Landslide).
- 324 - Land deformation in Grarem first detected by DInSAR, was confirmed by a site visit, during which small cracks were
325 visible on the ground (incoherent boundary region). Due to incoherent boundaries and because the displacement is
326 probably larger than what can be measured by one interferogram (depending on the wavelength, 5 cm for Sentinel-1), the
327 deformation measurements in this case are not reliable and accurate.
- 328 - Another landslide detected by InSAR in the Azeba region (6 km east of Mila) was visited too: the area covers 0.42 km²
329 and the site investigation (Fig. 20) confirms the landslide.
- 330 - Analysis with LiCSBAS revealed new hillside deformation (subsidence) which is probably a consequence of the mass
331 that moved in the main landslide hillside. Displacements time series, in Grarem region at some point, show deformation
332 along LOS with velocities ranging from 6 mm/year to 67 mm/year. This method is preferable in the large-scale area and
333 large-period analysis.



334
335 **Figure 20.** Landslide occurred in Azeba region (2 km North) detected by InSAR: (a) & (b)- visible ground cracks, (c)- coherence map of
336 Azeba zone delimited by the cracks.
337

338 5 Conclusions and Recommendations

339 In this paper, active and passive space-based satellite data are used to monitor and study the impact of natural hazards
340 (earthquakes and landslides) on struck areas. The C-band Sentinel-1 SAR datasets (active sensing) and optical images of
341 Sentinel-2 data (10 m spatial resolution) were used in this study to investigate the area, the passive images were used to validate
342 the active results. For the InSAR processing, the use of DInSAR, CCD methods and the LiCSBAS tool has been able to
343 generate a detailed time series analysis of ground changes.

344 InSAR techniques can extract useful geodetic information, such as the ground movement and track surface deformation over
345 large areas with centimetric accuracy in coherent change cases. The present research study has demonstrated that the InSAR
346 processing is adapted to study earthquake and landslides zones. As a result, three primary land failures were detected over the
347 study area using InSAR.

348 DInSAR is poorly suited to track and detected landslides. It is represented as a pixel decorrelation in phase interferograms and
349 high decay in coherence values. CCD is further suitable to map earthquake-induced landslides that may remain undetected
350 using coherent methods (DInSAR). The estimation of their horizontal displacement is a challenge to be inferred.

351 The Grarem deformation looks as a landslide that has just been initiated, but might extend under an upcoming triggering event.
352 Actually, the failure plane rim is presented as a dark line in the coherence map or as the circumference of the fringe in phase
353 maps (estimated area 3.94 sq. km). This impending land failure needs therefore a thorough and real-time monitoring and



354 adequate geotechnical studies. PS-InSAR can serve as an efficient and low-cost monitoring method able to obtain millimeter-
355 level precision displacement measurements over selected points in the area (Jia et al., 2019).
356 It is worth to increase awareness of possible future geotechnical threats in a timely manner, through on-site monitoring using
357 GPS, crack meters, and by placing inclinometers in the Grarem area, in order to develop a model of the slope stability.

358 **Acknowledgments:** In this work, we used SNAP and QGIS to analyze and plot maps. ESA, Copernicus, and COMET for
359 providing Sentinel data. The authors are grateful to European Space Agency (ESA) for providing freely the data through
360 Copernicus Program.

361 **Conflicts of Interest:** The authors declare no conflict of interest.

362 References

- 363 ASF DAAC: Alaska Satellite Facility, Available from: <https://search.asf.alaska.edu/#/> (Accessed 26 June 2021).
- 364 Bakon, M., Perissin, D., Lazecky, M. and Papco, J.: Infrastructure Non-linear Deformation Monitoring Via Satellite Radar
365 Interferometry, *Procedia Technol.*, 16, 294–300, doi:10.1016/j.protcy.2014.10.095, 2014.
- 366 Braun, A.: Radar satellite imagery for humanitarian response: Bridging the gap between technology and application, , 225
367 Available from: [https://publikationen.uni-tuebingen.de/xmlui/bitstream/handle/10900/91317/Braun 2019 Radar satellite
368 imagery for humanitarian response UB.pdf?sequence=1](https://publikationen.uni-tuebingen.de/xmlui/bitstream/handle/10900/91317/Braun%202019%20Radar%20satellite%20imagery%20for%20humanitarian%20response%20UB.pdf?sequence=1), 2019.
- 369 Canaslan Çomut, F., Gürboğa, Ş. and Smail, T.: Estimation of co-seismic land deformation due to Mw 7.3 2017 earthquake
370 in Iran (12 November 2017) using Sentinel-1 DInSAR, *Bull. Miner. Res. Explor.*, 162(August), 11–30,
371 doi:10.19111/bulletinofmre.604026, 2020.
- 372 Cascini, L., Peduto, D., Pisciotta, G., Arena, L., Ferlisi, S. and Fornaro, G.: The combination of DInSAR and facility damage
373 data for the updating of slow-moving landslide inventory maps at medium scale, *Nat. Hazards Earth Syst. Sci.*, 13(6), 1527–
374 1549, doi:10.5194/nhess-13-1527-2013, 2013.
- 375 ESA: ESA’s radar observatory mission for GMES operational services. Available from:
376 https://sentinel.esa.int/documents/247904/349449/S1_SP-1322_1.pdf, 2012.
- 377 ESA: Resolution and Swath - Sentinel-1 - Missions - Sentinel Online - Sentinel, Available from:
378 <https://sentinel.esa.int/web/sentinel/missions/sentinel-1/instrument-payload/resolution-swath> (Accessed 26 June 2021a).
- 379 ESA: SAR Instrument - Sentinel-1 SAR Technical Guide - Sentinel Online - Sentinel, Available from:
380 <https://sentinels.copernicus.eu/web/sentinel/technical-guides/sentinel-1-sar/sar-instrument> (Accessed 26 June 2021b).
- 381 Galve, J. P., Castañeda, C. and Gutiérrez, F.: Railway deformation detected by DInSAR over active sinkholes in the Ebro
382 Valley evaporite karst, Spain, *Nat. Hazards Earth Syst. Sci.*, 15(11), 2439–2448, doi:10.5194/nhess-15-2439-2015, 2015.
- 383 Goudarzi, M. a: Detection and measurement of land deformations caused by seismic events using InSAR, Sub-pixel
384 correlation, and Inversion techniques, , (January), 127, 2010.
- 385 Herrera, G., Fernández, J. A., Tomás, R., Cooksley, G. and Mulas, J.: Advanced interpretation of subsidence in Murcia (SE
386 Spain) using A-DInSAR data - Modelling and validation, *Nat. Hazards Earth Syst. Sci.*, 9(3), 647–661, doi:10.5194/nhess-9-
387 647-2009, 2009.
- 388 Hooper, A., Zebker, H., Segall, P. and Kampes, B.: A new method for measuring deformation on volcanoes and other natural
389 terrains using InSAR persistent scatterers, *Geophys. Res. Lett.*, 31(23), 1–5, doi:10.1029/2004GL021737, 2004.
- 390 Jacquemart, M. and Tiampo, K.: Leveraging time series analysis of radar coherence and normalized difference vegetation
391 index ratios to characterize pre-failure activity of the Mud Creek landslide, California, *Nat. Hazards Earth Syst. Sci.*, 21(2),
392 629–642, doi:10.5194/nhess-21-629-2021, 2021.
- 393 Jia, H., Zhang, H., Liu, L. and Liu, G.: Landslide deformation monitoring by adaptive distributed scatterer interferometric



- 394 synthetic aperture radar, *Remote Sens.*, 11(19), 1–18, doi:10.3390/rs11192273, 2019.
- 395 Jung, J. and Yun, S. H.: Evaluation of coherent and incoherent landslide detection methods based on synthetic aperture radar
396 for rapid response: A case study for the 2018 Hokkaido landslides, *Remote Sens.*, 12(2), 1–26, doi:10.3390/rs12020265,
397 2020.
- 398 Kim, J. W.: Applications of Synthetic Aperture Radar (SAR)/ SAR Interferometry (InSAR) for Monitoring of Wetland
399 Water Level and Land Subsidence, *Ohio State Univ.*, (503), 1–111, 2013.
- 400 Lazecký, M., Hatton, E., González, P. J., Hlaváčová, I., Jiráňková, E., Dvořák, F., Šustr, Z. and Martinovič, J.:
401 Displacements monitoring over Czechia by IT4S1 system for automatised interferometric measurements using Sentinel-1
402 data, *Remote Sens.*, 12(18), 1–21, doi:10.3390/RS12182960, 2020a.
- 403 Lazecký, M., Spaans, K., González, P. J., Maghsoudi, Y., Morishita, Y., Albino, F., Elliott, J., Greenall, N., Hatton, E.,
404 Hooper, A., Juncu, D., McDougall, A., Walters, R. J., Watson, C. S., Weiss, J. R. and Wright, T. J.: LiCSAR: An automatic
405 InSAR tool for measuring and monitoring tectonic and volcanic activity, *Remote Sens.*, 12(15), doi:10.3390/RS12152430,
406 2020b.
- 407 LNHC: Laboratoire National de l’Habitat et de la Construction, LNHC Available from: <http://lnhc-dz.com/> (Accessed 26
408 June 2021).
- 409 Meng, Q., Confuorto, P., Peng, Y., Raspini, F., Bianchini, S., Han, S., Liu, H. and Casagli, N.: Regional recognition and
410 classification of active loess landslides using two-dimensional deformation derived from sentinel-1 interferometric radar
411 data, *Remote Sens.*, 12(10), doi:10.3390/rs12101541, 2020.
- 412 Morishita, Y.: Nationwide urban ground deformation monitoring in Japan using Sentinel-1 LiCSAR products and LiCSBAS,
413 *Prog. Earth Planet. Sci.*, 8(1), doi:10.1186/s40645-020-00402-7, 2021.
- 414 Netzband, M., Stefanov, W. L. and Redman, C.: Applied remote sensing for urban planning, governance and sustainability.,
415 2007.
- 416 Pawluszek-Filipiak, K. and Borkowski, A.: Integration of DInSAR and SBAS techniques to determine mining-related
417 deformations using Sentinel-1 data: The case study of rydułtowy mine in Poland, *Remote Sens.*, 12(2),
418 doi:10.3390/rs12020242, 2020.
- 419 Rapant, P., Struhár, J. and Lazecký, M.: Radar interferometry as a comprehensive tool for monitoring the fault activity in the
420 vicinity of underground gas storage facilities, *Remote Sens.*, 12(2), doi:10.3390/rs12020271, 2020.
- 421 Roque, D., Perissin, D., Falcão, A. P., Fonseca, A. M. and Maria, J.: Dams regional safety warning using time-series insar
422 techniques, *Second Internatinal Dam World Conf.*, 21–24, 2015.
- 423 Sanabria, M. P., Guardiola-Albert, C., Tomás, R., Herrera, G., Prieto, A., Sánchez, H. and Tessitore, S.: Subsidence activity
424 maps derived from DInSAR data: Orihuela case study, *Nat. Hazards Earth Syst. Sci.*, 14(5), 1341–1360, doi:10.5194/nhess-
425 14-1341-2014, 2014.
- 426 Tampuu, T., Praks, J., Uiboupin, R. and Kull, A.: Long term interferometric temporal coherence and DInSAR phase in
427 Northern Peatlands, *Remote Sens.*, 12(10), 7–9, doi:10.3390/rs12101566, 2020.
- 428 Tzouvaras, M., Danezis, C. and Hadjimitsis, D. G.: Small scale landslide detection using Sentinel-1 interferometric SAR
429 coherence, *Remote Sens.*, 12(10), doi:10.3390/rs12101560, 2020.
- 430 USGS: M 5.0 - 3 km NNE of Sidi Mérouane, Algeria, Available from:
431 <https://earthquake.usgs.gov/earthquakes/eventpage/us6000bag6/executive> (Accessed 26 June 2021).
- 432 Wang, Z., Li, Z. and Mills, J.: A new approach to selecting coherent pixels for ground-based SAR deformation monitoring,
433 *ISPRS J. Photogramm. Remote Sens.*, 144, 412–422, doi:10.1016/j.isprsjprs.2018.08.008, 2018.
- 434 WWO: Mila, Mila, Algeria Historical Weather Almanac, Available from: [https://www.worldweatheronline.com/mila-
435 weather-history/mila/dz.aspx](https://www.worldweatheronline.com/mila-weather-history/mila/dz.aspx) / (Accessed 26 June 2021).
- 436